Self-consistent calculation of hole mobilities in narrow-gap $Hg_{0.8}Cd_{0.2}Te$

R. Grill
Institute of Physics, Charles University, Ke Karlovu 5, CS-121 16 Prague 2, Czechoslovakia
(Received 25 September 1991; revised manuscript received 9 March 1992)

The Kadanoff-Baym Green-function formalism is used to calculate the heavy- and light-hole mobilities in p-type $Hg_{1-x}Cd_xTe$ ($x=0.2$). The polar-optical-phonon and charged-impurity scatterings are included in the self-consistent Born approximation. A comparison with a Boltzmann-equation calculation is made. Significant corrections are found.

I. INTRODUCTION

Calculations of the heavy- and light-hole mobilities are frequently given in papers on $A^{III}B^{V}$ and $A^{II}B^{VI}$ semiconductors. Nevertheless, there are two serious causes of concern that stimulate continued research in this problem. First, although most of the calculational methods used are based essentially on the Boltzmann equation (BE), the Peierls-Landau conditions of the validity of the BE are not fulfilled in most of these materials and application of the BE is thus not justified. Second, the relative light-hole mobility (with respect to the heavy-hole one) in narrow-gap semiconductors is too high on the basis of the BE results, and, moreover, the calculated magnetic-field dependence of the Hall constant does not provide satisfactory agreement with experiment.[1]

This paper is devoted to a calculation of the drift hole mobilities of narrow-gap polar semiconductors by a method of solving the Kadanoff-Baym kinetic equation (KBE).[2] There are two necessary steps to obtain satisfactory results. The first one is a determination of the equilibrium Green function as well as the density of states (DOS) and the occupation rate. The second one is the substitution of the equilibrium Green function into the kinetic equation and its solution. This treatment yields the Wigner distribution function and the hole mobilities. An ensuing comparison of the obtained results with those of the Boltzmann-equation treatment is found to be very instructive.

II. HAMILTONIAN

All the following calculations will start from the Hamiltonian given in the form

$$\begin{aligned}\mathcal{H}&=\mathcal{H}_e+\mathcal{H}_{\rm ph}+\mathcal{H}_{e\text{-}i}+\mathcal{H}_{e\text{-ph}}\\&\equiv\sum_{j,\mathbf{k},\sigma}E_{j\mathbf{k}}a^{\dagger}_{j\mathbf{k}\sigma}a_{j\mathbf{k}\sigma}+\sum_{\mathbf{q}}\omega_{\mathbf{q}}b^{\dagger}_{\mathbf{q}}b_{\mathbf{q}}+\sum_{\substack{\mathbf{k},\mathbf{q}\\(\mathbf{k}\neq\mathbf{q})}}\sum_{i,j\,\sigma,\sigma'}V(\mathbf{k},i,\sigma,\mathbf{q},j,\sigma')a^{\dagger}_{j\mathbf{q}\sigma'}a_{i\mathbf{k}\sigma}\\&\quad+\sum_{\mathbf{k},\mathbf{q}}\sum_{i,j}\sum_{\sigma,\sigma'}M(\mathbf{k},i,\sigma,\mathbf{q},j,\sigma')a^{\dagger}_{j\mathbf{q}\sigma'}a_{i\mathbf{k}\sigma}[b^{\dagger}_{\mathbf{k}-\mathbf{q}}+b_{\mathbf{q}-\mathbf{k}}]\,.\end{aligned}\tag{1}$$

$\mathcal{H}_e$, $\mathcal{H}_{\rm ph}$, $\mathcal{H}_{e\text{-}i}$, and $\mathcal{H}_{e\text{-ph}}$ are nonperturbed electron and phonon Hamiltonians and charged-impurity and electron-phonon interactions, respectively. $\mathbf{k},\mathbf{q}$ are wave vectors, σ,σ' are spin indices, i,j are band indices (equal to 1 for the heavy-hole band and 2 for the light-hole one), and $a^{\dagger}_{j\mathbf{k}\sigma}$, $b^{\dagger}_{\mathbf{q}}$, $a_{j\mathbf{k}\sigma}$, $b_{\mathbf{q}}$ are the hole and phonon creation and annihilation operators, respectively. The phonon frequency $\omega_{\mathbf{q}}$ is taken to be constant $\omega_{\mathbf{q}}=\omega_0$. (We set $\hbar=1$ throughout this paper.) The hole energy $E_{j\mathbf{k}}$ is taken from the Kane model[3]

$$E_{1\mathbf{k}}=\frac{k^2}{2m_1^*}\,,\tag{2}$$

$$E_{2\mathbf{k}}=\frac{E_g}{2}\left[\left[1+\frac{2k^2}{m_2^*E_g}\right]^{1/2}-1\right].\tag{3}$$

Here E_g,m_1^*,m_2^* are the energy gap and the heavy-hole and light-hole effective masses, respectively. V is the charged-impurity screened Coulomb potential

$$V(\mathbf{k},i,\sigma,\mathbf{q},j,\sigma')=\sum_{\delta}\frac{Z_\delta e}{\epsilon_s\epsilon_0\left[|\mathbf{k}-\mathbf{q}|^2+\frac{1}{d_{Ds}^2}\right]}e^{-i(\mathbf{k}-\mathbf{q})\mathbf{R}_\delta}\int u^{\dagger}_{\sigma'\mathbf{q}j}(\mathbf{r})u_{\sigma\mathbf{k}i}(\mathbf{r})d\mathbf{r}\,,\tag{4}$$

where

$$d_{Ds}^2=\frac{\epsilon_0\epsilon_s}{\beta e^2 p^*} \tag{5}$$

and M is the potential of the screened electron-phonon interaction

$$M(\mathbf{k},i,\sigma,\mathbf{q},j,\sigma')=\left[\frac{\omega_0 e^2}{2\epsilon_0\left[|\mathbf{k}-\mathbf{q}|^2+\frac{1}{d_{D_\infty}^2}\right]}\left[\frac{1}{\epsilon_\infty}-\frac{1}{\epsilon_s}\right]\right]^{1/2}\int u^\dagger_{\sigma'\mathbf{q}j}(\mathbf{r})u_{\sigma\mathbf{k}i}(\mathbf{r})d\mathbf{r}\ , \tag{6}$$

$$d_{D_\infty}^2=\frac{\epsilon_0\epsilon_\infty}{\beta e^2 p'}\ . \tag{7}$$

$Z_\vartheta(=\pm e),\mathbf{R}_\vartheta,\epsilon_0,\epsilon_s,\epsilon_\infty$ are the charge and the position of the ϑth scattering center and vacuum, static and high-frequency dielectric constants, respectively. d_{Ds} and d_{D_∞} are the Debye screening lengths and $\beta=1/k_BT$. The concentrations p' and p^* are as usual given by

$$p'=\int_{-\infty}^{\infty}[\mathcal{D}(1,E)+\mathcal{D}(2,E)]f_0(1-f_0)dE\ , \tag{8}$$

$$p^*=p'+N_A^-\left[1-\frac{N_A^-}{N_A}\right]\ , \tag{9}$$

where $\mathcal{D}(1,E)$ and $\mathcal{D}(2,E)$ are the heavy- and light-hole DOS and N_A and N_A^- are the total and ionized acceptor concentrations. f_0 is the Fermi-Dirac function

$$f_0=1/\{1+\exp[\beta(E-E_F)]\}\ , \tag{10}$$

E_F is the Fermi energy. The integrals in (4) and (6) measure the overlap between the periodic parts $u_{\sigma\mathbf{k}i}(\mathbf{r})$ of the Bloch functions.[4] For the purpose of the next calculations, it is necessary to determine the overlap function

$$\mathcal{G}_{ij}(\vartheta)\equiv\mathcal{G}_{ij}(\mathbf{k},\mathbf{k}')=\tfrac{1}{2}\sum_{\sigma,\sigma'}\left|\int u^\dagger_{\sigma'\mathbf{k}'j}(\mathbf{r})u_{\sigma\mathbf{k}i}(\mathbf{r})d\mathbf{r}\right|^2\ , \tag{11}$$

where ϑ is the angle between $\mathbf{k}$ and $\mathbf{k}'$. For p-like wave functions it is taken according to Ref. 5 as

$$\mathcal{G}_{11}(\vartheta)=\mathcal{G}_{22}(\vartheta)=\tfrac{1}{4}(1+3\cos^2\vartheta)\ , \tag{12}$$

$$\mathcal{G}_{12}(\vartheta)=\mathcal{G}_{21}(\vartheta)=\tfrac{3}{4}\sin^2\vartheta\ . \tag{13}$$

III. EQUILIBRIUM GREEN FUNCTIONS

A critical point of the Green-function calculation is the choice of the self-energy approximation. Here the self-consistent Born approximation is used. The self-energies $\Sigma^<,\Sigma^>$ are then given in the form

$$\Sigma^<(i,\mathbf{k},\omega)=\tfrac{1}{2}\sum_{\mathbf{q}}\sum_{j}\sum_{\sigma,\sigma'}\{|V(\mathbf{k},i,\sigma,\mathbf{q},j,\sigma')|^2G^<(j,\mathbf{q},\omega)+|M(\mathbf{k},i,\sigma,\mathbf{q},j,\sigma')|^2[(N_q+1)G^<(j,\mathbf{q},\omega+\omega_0)+N_qG^<(j,\mathbf{q},\omega-\omega_0)]\}\ , \tag{14}$$

$$\Sigma^>(i,\mathbf{k},\omega)=\tfrac{1}{2}\sum_{\mathbf{q}}\sum_{j}\sum_{\sigma,\sigma'}\{|V(\mathbf{k},i,\sigma,\mathbf{q},j,\sigma')|^2G^>(j,\mathbf{q},\omega)+|M(\mathbf{k},i,\sigma,\mathbf{q},j,\sigma')|^2[(N_q+1)G^>(j,\mathbf{q},\omega-\omega_0)+N_qG^>(j,\mathbf{q},\omega+\omega_0)]\}\ . \tag{15}$$

N_q is the mean phonon occupation number $N_q=1/[\exp(\beta\omega_0)-1]$.

Applying the standard Green-function formalism,[6] one obtains

$$A(j,k,\omega)=\frac{2\Gamma}{(\omega-E_{jk}-\mathrm{Re}\Sigma^r)^2+\Gamma^2}\ , \tag{16}$$

$$G^<=\imath f_0A,\quad G^>=-\imath(1-f_0)A,\quad \Sigma^<=2\imath f_0\Gamma,\quad \Sigma^>=-2\imath(1-f_0)\Gamma\ , \tag{17}$$

$$\mathrm{Re}\Sigma^r(j,k,\omega)=\frac{1}{\pi}\int_{-\infty}^{\infty}dz\frac{\Gamma(j,k,z)}{\omega-z}\ , \tag{17'}$$

which, together with (14) and (15), forms the complete set of equations to be solved. Here A is the spectral density function and $\Gamma=-\mathrm{Im}\Sigma^r>0$.

After integration of (14) and (15) and substituting (17) the numerically solvable system reads as[7]

$$\Gamma(i,\varepsilon,\omega)=\sum_{l=1}^{4}\Gamma_l(i,\varepsilon,\omega)\ , \tag{18}$$

$$\Gamma_1(i,\varepsilon,\omega)=\frac{C_i^1}{\varepsilon}\int_0^\infty\frac{d\varepsilon'}{\sqrt{\varepsilon'}}f_1\left[\frac{\varepsilon+\varepsilon'+C_i^5}{2\sqrt{\varepsilon\varepsilon'}}\right]A(i,\varepsilon',\omega)\ , \tag{19}$$

$$\Gamma_2(i,\varepsilon,\omega)=\frac{C_i^2}{\varepsilon}\int_0^\infty \frac{d\varepsilon'}{\sqrt{\varepsilon'}} f_2\left[\frac{\chi_i\varepsilon+\varepsilon'+C_j^5}{2\sqrt{\chi_i\varepsilon\varepsilon'}}\right] A(j,\varepsilon',\omega), \tag{20}$$

$$\Gamma_3(i,\varepsilon,\omega)=\frac{C_i^3}{\sqrt{\varepsilon}}\int_0^\infty d\varepsilon' f_3\left[\frac{\varepsilon+\varepsilon'}{2\sqrt{\varepsilon\varepsilon'}},\frac{\varepsilon+\varepsilon'+C_i^6}{2\sqrt{\varepsilon\varepsilon'}}\right] \times\{[N_q+f_0(\omega+\omega_0)]A(i,\varepsilon',\omega+\omega_0)+[N_q+1-f_0(\omega-\omega_0)]A(i,\varepsilon',\omega-\omega_0)\}\ , \tag{21}$$

$$\Gamma_4(i,\varepsilon,\omega)=\frac{C_i^4}{\sqrt{\varepsilon}}\int_0^\infty d\varepsilon' f_4\left[\frac{\chi_i\varepsilon+\varepsilon'}{2\sqrt{\chi_i\varepsilon\varepsilon'}},\frac{\chi_i\varepsilon+\varepsilon'+C_j^6}{2\sqrt{\chi_i\varepsilon\varepsilon'}}\right] \times\{[N_q+f_0(\omega+\omega_0)]A(j,\varepsilon',\omega+\omega_0)+[N_q+1-f_0(\omega-\omega_0)]A(j,\varepsilon',\omega-\omega_0)\}\ , \tag{22}$$

$$f_1(a)=\frac{6a^2-2}{a^2-1}-3a\ln\left[\frac{a+1}{a-1}\right],\quad f_2(a)=a\ln\left[\frac{a+1}{a-1}\right]-2\ ,$$

$$f_3(a,b)=8\frac{a-b}{b^2-1}+(9b^2-6ab+1)\ln\left[\frac{b+1}{b-1}\right]-18b+12a\ ,$$

$$f_4(a,b)=(1+2ab-3b^2)\ln\left[\frac{b+1}{b-1}\right]+6b-4a\ ,$$

$$\chi_i=\frac{m_i^*}{m_j^*},\quad C_i^1=\frac{e^4}{128\sqrt{2}\pi^2\epsilon_0^2}\frac{n_i}{\epsilon_s^2\sqrt{m_i^*}},\quad C_i^2=\frac{3}{\sqrt{\chi_i}}C_i^1,\quad C_i^5=\frac{1}{2d_{Ds}^2 m_i^*}\ ,$$

$$C_i^3=\frac{e^2}{128\sqrt{2}\pi^2\epsilon_0}\omega_0\sqrt{m_i^*}\left[\frac{1}{\epsilon_\infty}-\frac{1}{\epsilon_s}\right],\quad C_i^4=\frac{3}{\chi_i}C_i^3,\quad C_i^6=\frac{1}{2d_{D_\infty}^2 m_i^*},\quad i\neq j\ .$$

n_i is the charged-impurity concentration. Here Γ_1, Γ_2, Γ_3, and Γ_4 represent the intraband impurity, the interband impurity, the intraband optical phonon, and the interband optical phonon contributions, respectively.

For numerical purposes it has been useful to transform the wave-vector dependence into energy variable ε so that

$$E_{1k}\to E_{1\varepsilon}=\varepsilon,\quad \varepsilon=\frac{k^2}{2m_1^*}\ ,$$

for the heavy-hole band and

$$E_{2k}\to E_{2\varepsilon}=\frac{E_g}{2}[(1+4\varepsilon/E_g)^{1/2}-1],\quad \varepsilon=\frac{k^2}{2m_2^*}\ ,$$

for the light-hole one.

The DOS is calculated from

$$\mathcal{D}(i,\omega)=C_i^7\int_0^\infty d\varepsilon\sqrt{\varepsilon}\,A(i,\varepsilon,\omega)\ ,\qquad C_i^7=\frac{1}{\sqrt{2}}\left[\frac{\sqrt{m_i^*}}{\pi}\right]^3\ , \tag{23}$$

and occupation rate (probability)

$$\mathcal{P}(i,\omega)=\frac{\mathcal{D}(i,\omega)f_0}{\int_{-\infty}^\infty \mathcal{D}(i,x)f_0 dx}\ . \tag{24}$$

IV. KADANOFF-BAYM KINETIC EQUATION IN AN EXTERNAL FIELD

The KBE in the electric field is taken in the form[6]

$$eA^2\frac{\partial f_0}{\partial\omega}\mathcal{E}\cdot[(\nabla_k E_{ik}+\nabla_k \mathrm{Re}\Sigma^r)\Gamma+(\omega-E_{ik}-\mathrm{Re}\Sigma^r)\nabla_k\Gamma]=-i(\Sigma^<A-2\Gamma G^<)\ . \tag{25}$$

(Corrections reported in Ref. 8 disappear in our Born approximation.)

Passing from k to ε the KBE is rewritten as

$$e|\mathcal{E}|\left[\frac{2\varepsilon}{m_i^*}\right]^{1/2}\cos\phi\frac{\partial f_0}{\partial\omega}A^2\Gamma^2\frac{\partial}{\partial\varepsilon}\left[\frac{E_{i\varepsilon}+\mathrm{Re}\Sigma^r-\omega}{\Gamma}\right]=-i(\Sigma^<A-2\Gamma G^<)\ , \tag{26}$$

$$\cos\phi=\frac{\mathbf{k}\cdot\mathcal{E}}{k|\mathcal{E}|}\ .$$

Next the Green function of $G^<$ and the self-energy $\Sigma^<$ are divided into two parts

$$G^<=G^<(\mathcal{E}=0)+\delta G^<,\quad \Sigma^<=\Sigma^<(\mathcal{E}=0)+\delta\Sigma^< , \tag{27}$$

where the first parts are the equilibrium functions and the second ones are small changes due to the nonequilibrium. Substituting (27) into (26) the equilibrium functions disappear and the KBE takes the form

$$-i\delta G^<=\left\{\frac{e|\mathcal{E}|}{\sqrt{2m_i^*}}\left[-\frac{\partial f_0}{\partial\omega}\right](\cos\phi)\mathcal{F}-i\frac{\delta\Sigma^< A}{2\Gamma}\right\}, \tag{28}$$

where

$$\mathcal{F}(i,\varepsilon,\omega)=A^2\Gamma\sqrt{\varepsilon}\frac{\partial}{\partial\varepsilon}\left[\frac{E_{i\varepsilon}+\mathrm{Re}\Sigma^r-\omega}{\Gamma}\right] . \tag{29}$$

Now one more transformation is useful to define

$$-i\delta G^<=\frac{e|\mathcal{E}|}{\sqrt{2m_i^*}}\left[-\frac{\partial f_0}{\partial\omega}\right]\cos\phi[\mathcal{F}+A\delta f(i,\varepsilon,\omega)] . \tag{30}$$

The new function δf has good properties for the numerical treatment. Applying the self-energy form (14), the self-consistent equation for δf is obtained,

$$\delta f(i,\varepsilon,\omega)=\frac{1}{\Gamma\left[-\dfrac{\partial f_0(\omega)}{\partial\omega}\right]}\sum_{l=1}^{4}\delta f_l(i,\varepsilon,\omega) , \tag{31}$$

$$\delta f_1(i,\varepsilon,\omega)=\frac{C_i^1}{\varepsilon}\left[-\frac{\partial f_0(\omega)}{\partial\omega}\right]\int_0^\infty d\varepsilon'\frac{1}{\sqrt{\varepsilon'}}\mathcal{I}_1\left[\frac{\varepsilon+\varepsilon'+C_i^5}{2\sqrt{\varepsilon\varepsilon'}}\right][\mathcal{F}(i,\varepsilon',\omega)+A(i,\varepsilon',\omega)\delta f(i,\varepsilon',\omega)] , \tag{32}$$

$$\delta f_2(i,\varepsilon,\omega)=\frac{C_i^2}{\varepsilon}\sqrt{\chi_i}\left[-\frac{\partial f_0(\omega)}{\partial\omega}\right]\int_0^\infty d\varepsilon'\frac{1}{\sqrt{\varepsilon'}}\mathcal{I}_2\left[\frac{\chi_i\varepsilon+\varepsilon'+C_j^5}{2\sqrt{\chi_i\varepsilon\varepsilon'}}\right][\mathcal{F}(j,\varepsilon',\omega)+A(j,\varepsilon',\omega)\delta f(j,\varepsilon',\omega)] , \tag{33}$$

$$\begin{aligned}\delta f_3(i,\varepsilon,\omega)=&\frac{C_i^3}{\sqrt{\varepsilon}}\int_0^\infty d\varepsilon'\mathcal{I}_3\left[\frac{\varepsilon+\varepsilon'}{2\sqrt{\varepsilon\varepsilon'}},\frac{\varepsilon+\varepsilon'+C_i^6}{2\sqrt{\varepsilon\varepsilon'}}\right]\\&\times\left\{[N_q+1]\left[-\frac{\partial f_0(\omega+\omega_0)}{\partial\omega}\right][\mathcal{F}(i,\varepsilon',\omega+\omega_0)+A(i,\varepsilon',\omega+\omega_0)\delta f(i,\varepsilon',\omega+\omega_0)]\right.\\&\left.+N_q\left[-\frac{\partial f_0(\omega-\omega_0)}{\partial\omega}\right][\mathcal{F}(i,\varepsilon',\omega-\omega_0)+A(i,\varepsilon',\omega-\omega_0)\delta f(i,\varepsilon',\omega-\omega_0)]\right\} ,\end{aligned} \tag{34}$$

$$\begin{aligned}\delta f_4(i,\varepsilon,\omega)=&\frac{C_i^4}{\sqrt{\varepsilon}}\sqrt{\chi_i}\int_0^\infty d\varepsilon'\mathcal{I}_4\left[\frac{\chi_i\varepsilon+\varepsilon'}{2\sqrt{\chi_i\varepsilon\varepsilon'}},\frac{\chi_i\varepsilon+\varepsilon'+C_j^6}{2\sqrt{\chi_i\varepsilon\varepsilon'}}\right]\\&\times\left\{[N_q+1]\left[-\frac{\partial f_0(\omega+\omega_0)}{\partial\omega}\right][\mathcal{F}(j,\varepsilon',\omega+\omega_0)+A(j,\varepsilon',\omega+\omega_0)\delta f(j,\varepsilon',\omega+\omega_0)]\right.\\&\left.+N_q\left[-\frac{\partial f_0(\omega-\omega_0)}{\partial\omega}\right][\mathcal{F}(j,\varepsilon',\omega-\omega_0)+A(j,\varepsilon',\omega-\omega_0)\delta f(j,\varepsilon',\omega-\omega_0)]\right\} ,\end{aligned} \tag{35}$$

$$\mathcal{I}_1(a)=\frac{a(9a^2-5)}{a^2-1}-(4.5a^2+0.5)\ln\left[\frac{a+1}{a-1}\right] ,$$

$$\mathcal{I}_2(a)=(1.5a^2-0.5)\ln\left[\frac{a+1}{a-1}\right]-3a ,$$

$$\mathcal{I}_3(a,b)=b(a-b)\frac{6b^2+2}{b^2-1}-[a(9b^2+1)-b(12b^2+2)]\ln\left[\frac{b+1}{b-1}\right]-18b^2+12ab-4 ,$$

$$\mathcal{I}_4(a,b)=[a(3b^2-1)-b(4b^2-2)]\ln\left[\frac{b+1}{b-1}\right]+8b^2-6ab-\tfrac{4}{3},\quad i\neq j .$$

Constants C_i^l and χ_i are the same as those given in Sec. III. Interpretation of δf_1, δf_2, δf_3, and δf_4 is analogous to that of Γ_1, Γ_2, Γ_3, and Γ_4 above. Having δf, the drift mobility $\mu(i)$ is calculated from

TABLE I. Input parameters.

T (K)	E_g (meV)	m_2^*/m_0	p'(I) (10^{13}/cm^3)	p'(II) (10^{13}/cm^3)	p^*(I) (10^{15}/cm^3)	p^*(II) (10^{16}/cm^3)
10	61.6	4.47×10^{-3}	0.0108	0.0108	1.20	1.20
15	63.7	4.63×10^{-3}	0.943	0.949	1.21	1.20
20	64.8	4.70×10^{-3}	9.35	10.0	1.27	1.21
30	67.9	4.92×10^{-3}	68.7	117.0	1.66	1.29
40	71.1	5.15×10^{-3}	129.0	376.0	1.90	1.47
60	77.5	5.59×10^{-3}	178.0	974.0	1.99	1.79
80	83.9	6.04×10^{-3}	191.0	1370.0	2.00	1.92

$$\mu(i)=\frac{e\sqrt{m_i^*}}{3\sqrt{2}\pi^3 p(i)}\int_{-\infty}^{\infty}d\omega\left[-\frac{\partial f_0(\omega)}{\partial\omega}\right]\int_0^{\infty}d\varepsilon\frac{\partial E_{i\varepsilon}}{\partial\varepsilon}\varepsilon[\mathcal{F}(i,\varepsilon,\omega)+A(i,\varepsilon,\omega)\delta f(i,\varepsilon,\omega)]\ , \tag{36}$$

$p(i)$ being the particle density.

Analogically to the occupation rate (24) we define the conduction rate

$$\Xi(i,\omega)=\frac{\left[-\frac{\partial f_0(\omega)}{\partial\omega}\right]\int_0^{\infty}d\varepsilon\frac{\partial E_{i\varepsilon}}{\partial\varepsilon}\varepsilon[\mathcal{F}(i,\varepsilon,\omega)+A(i,\varepsilon,\omega)\delta f(i,\varepsilon,\omega)]}{\int_{-\infty}^{\infty}dx\left[-\frac{\partial f_0(x)}{\partial x}\right]\int_0^{\infty}d\varepsilon\frac{\partial E_{i\varepsilon}}{\partial\varepsilon}\varepsilon[\mathcal{F}(i,\varepsilon,x)+A(i,\varepsilon,x)\delta f(i,\varepsilon,x)]}\ . \tag{37}$$

V. THE LIMIT TO THE BOLTZMANN EQUATION

If the scattering processes can be taken as sufficiently weak, so that $\beta\Gamma\ll1$, the following limits in A are allowed:

$$A(i,\varepsilon,\omega)\to2\pi\delta(E_{i\varepsilon}-\omega),\quad A^2\Gamma\to2\pi\delta(E_{i\varepsilon}-\omega)\ . \tag{38}$$

Application of (38) to the DOS form (23) gives the classical Kane DOS

$$\mathcal{D}(1,E)=\frac{\sqrt{2}}{\pi^2}m_1^{*3/2}\sqrt{E}\ ,$$
$$\mathcal{D}(2,E)=\frac{\sqrt{2}}{\pi^2}m_2^{*3/2}\sqrt{E(1+E/E_g)}(1+2E/E_g)\ , \tag{39}$$

and the KBE is, in this limit, equivalent to the Boltzmann equation.

VI. KBE COMPUTATION FOR p-type $Hg_{1-x}Cd_xTe$

Our calculations have been performed for p-type $Hg_{1-x}Cd_xTe$ ($x=0.2$) by the iteration method on a half-plane ($\varepsilon>0,\omega$),[7] where Γ, $\mathrm{Re}\Sigma^r$, and δf have been tabulated. The input parameters have been taken mostly from Ref. 9. The optical-phonon energy has been taken as the energy of the dominant HgTe mode $\omega_0=17.1$ meV and the heavy-hole effective mass has been taken as $m_h^*=0.6m_0$. The concrete calculations have been performed at two model impurity concentrations $N_A=5\times10^{15}$ cm^{-3}, $N_D=3\times10^{15}$ cm^{-3} (hereafter designated as I) and $N_A=5\times10^{16}$ cm^{-3}, $N_D=3\times10^{16}$ cm^{-3} (designated II) and in the temperature range 10–80 K where p-type-like experimental transport data are available.[10] Temperature-dependent input parameters are given in Table I. (The concentrations p',p^* correspond to the case of parabolic band and acceptor activation energy 10 meV.) The Fermi level has been fixed so that the values of p' are the same as those in Table I. The charged-impurity concentration has been calculated for fully ionized donors from electric neutrality condition $n_i=N_D^+ +N_A^-=2N_D+p(1)+p(2)$.

VII. RESULTS AND DISCUSSION

The calculated heavy- and light-hole DOS for case I are shown in Figs. 1 and 2, respectively. The detailed

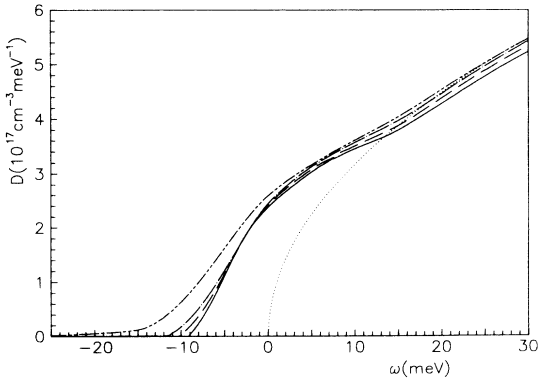

FIG. 1. The DOS of the heavy-hole band in case I ($N_A=5\times10^{15}$ cm^{-3}, $N_D=3\times10^{15}$ cm^{-3}). Temperatures 10, 20, 40, and 80 K correspond to line types ——, — — —, —·—·—·, ——··——, respectively. The dotted line shows the standard Kane DOS.

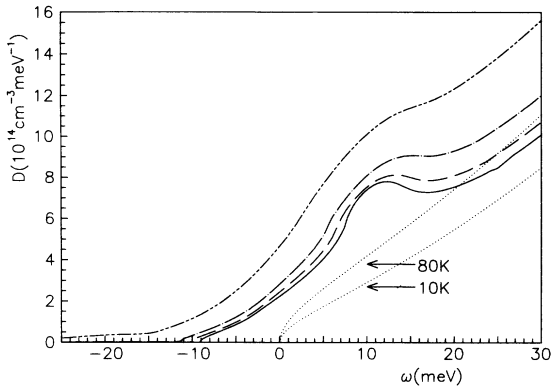

FIG. 2. The DOS of the light-hole band in case I. The meaning of the lines is identical to that in Fig. 1. Because of temperature dependence of the standard Kane light-hole DOS two limiting dotted lines for 10 and 80 K are given.

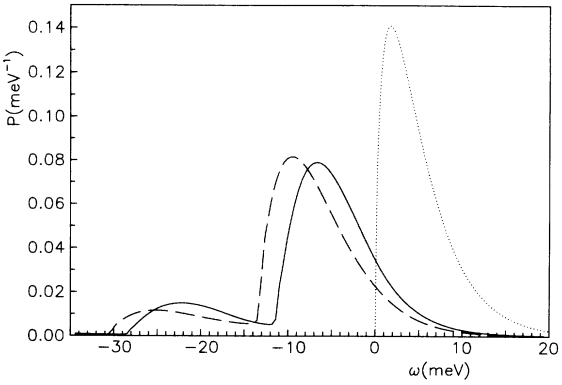

FIG. 4. Heavy-hole occupation rate at temperature 40 K. The solid and dashed lines correspond to cases I and II ($N_A=5\times10^{16}$ cm^{-3}, $N_D=3\times10^{16}$ cm^{-3}), respectively. The dotted line shows the standard occupation rate of the Kane shape of the band.

view of the heavy-hole band edge is plotted in Fig. 3. The results for case II do not contain qualitative changes against case I. Examples of heavy- and light-hole occupation rates (24) are given in Figs. 4 and 5. The dotted lines show the standard DOS and occupation rate functions based on the Kane shape of the bands.

Because of the renormalizing effects of the scattering processes, especially optical-phonon scattering, the band edge shifts to the gap and the polaron effect is seen. The influence of only impurity scattering on the DOS can be checked in Ref. 11 and is found here to be of minor importance in case I as well as II. Due to the interband scattering, the light-hole band is significantly changed and the polaron effect creates a bulge on the light-hole DOS. The phonon echoes of the band edge appear at distance $i\omega_0$ ($i=1,2,3,\ldots$) from the regular band edge (the steps on Fig. 3) and in spite of the small values of the DOS in tails a large part of the particles, especially the light holes, is, because of a strong increase of f_0, located on them (Figs. 4 and 5). Physically the echoes are due to a virtual phonon emission and absorption. They currently appear in self-consistent theories like the dynamical CPA (coherent potential approximation).[12,13] The DOS depends on the Fermi level position. At low temperatures the DOS has a local minimum in the vicinity of E_F.

The band tail must be influenced by the acceptor level (near the arrow to the solid line in Fig. 3) by a hybridization with the impurity states. Owing to the Born approximation used here, this effect is not included in this paper. The impurity concentrations in the calculations used are not so high as to change the transport results significantly. As is shown in Ref. 14, the impurity-band conduction has a substantial meaning above the impurity concentration $N_{\rm crit}\approx5\times10^{17}$ cm^{-3}.

Comparing to the Kane model the ratio $p(2)/p(1)$ significantly increases. The ratio $p(2)/p(1)$, the relative echos occupation r given by

$$r(i)=\int_{-\infty}^{E_b}\mathcal{P}(i,x)dx \tag{40}$$

(where E_b is band-edge energy taken at an inflection point of $\mathcal{P}$), and E_b are given in Table II. Figures 6–9 show examples of the self-energy functions Γ and $\mathrm{Re}\Sigma^r$.

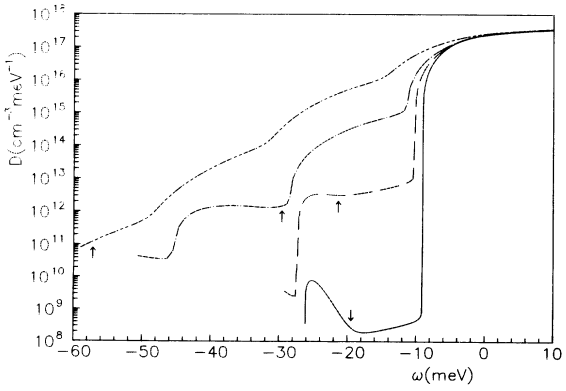

FIG. 3. The DOS in a detailed view of the heavy-hole band edge in case I. The meaning of the lines is identical to that in Fig. 1. The arrows point to the Fermi level position.

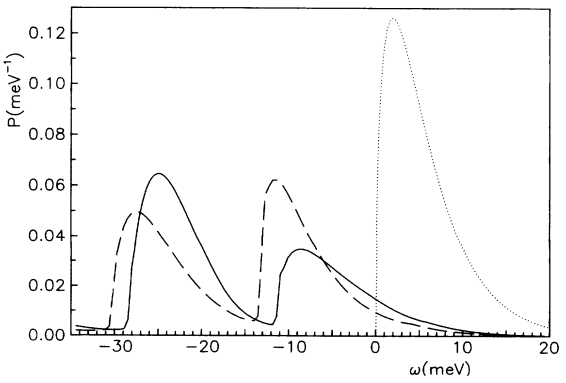

FIG. 5. Light-hole occupation rate at temperature 40 K. The meaning of the lines is identical to that in Fig. 4.

TABLE II. Ratio $p(2)/p(1)$ from the Green function and Kane model calculation, relative echoes occupation and band-edge position [$p(2)/p(1)$ is independent of the impurity concentration in the Kane model; the signs I,II, are defined in Sec. VI]. The Boltzmann regime corresponds to $r \ll 1$.

T (K)	Green functions $\frac{p(2,\mathrm{I})}{p(1,\mathrm{I})}$	Green functions $\frac{p(2,\mathrm{II})}{p(1,\mathrm{II})}$	Kane model $\frac{p(2)}{p(1)}$	r 1,I	r 2,I	r 1,II	r 2,II	E_b(I) (meV)	E_b(II) (meV)
10	37.8×10^{-4}	39.2×10^{-4}	6.82×10^{-4}	0.16	0.69	0.16	0.61	−9.1	−9.6
15	34.5×10^{-4}	38.6×10^{-4}	7.37×10^{-4}	0.17	0.70	0.16	0.58	−9.8	−10.8
20	30.3×10^{-4}	35.9×10^{-4}	7.72×10^{-4}	0.17	0.68	0.15	0.58	−10.2	−11.6
30	27.7×10^{-4}	32.0×10^{-4}	8.63×10^{-4}	0.18	0.65	0.16	0.51	−10.7	−12.7
40	27.3×10^{-4}	30.9×10^{-4}	9.61×10^{-4}	0.19	0.62	0.16	0.48	−11.3	−13.5
60	29.3×10^{-4}	31.7×10^{-4}	11.52×10^{-4}	0.20	0.57	0.15	0.46	−13.5	−16.0
80	32.3×10^{-4}	33.8×10^{-4}	13.14×10^{-4}	0.21	0.56	0.13	0.42	−15.0	−18.0

These functions illustrate that the light-hole band is strongly influenced by the interband scattering into the heavy-hole band while the intraband scattering has no importance in the light-hole band.

Results of the hole mobility calculations are given in Table III. Here the BE results are included, too. Comparing the KBE to the BE results, hole mobilities are seen to differ substantially. The minimal differences are in heavy-hole band at higher temperatures. This effect has a direct connection with the degree of perturbing the Peierls-Landau condition mentioned above.

Figures 10 and 11 show examples of the conduction rate. Similarly to the case of the DOS a large part of the transport processes is found to take place in the phonon echoes of the band edge. The relative echoes conductivity $\hat{r}$ given by

$$\hat{r}(i)=\int_{-\infty}^{E_b}\Xi(i,x)dx\ , \tag{41}$$

where E_b is the same as in (40), is given in Table IV.

A very instructive view of the light-hole transport is given by the topographical projection of the light-hole conduction density in the (ε,ω) plane, plotted in Figs. 12 and 13. We can see two considerably different areas there. Because of the backscattering from the heavy-hole band extensive areas of a relatively low conduction density appear in the large-ε region. In particular, at low temperatures they play a dominant role in the light-hole transport. On the contrary a small-ε region is distinguished by a sharp increase of the conduction density similar to the Boltzmann δ-function shape of this function. A contribution of these two areas to the transport can be found also in Figs. 10 and 11. Additional details may be found in Ref. 7.

Direct comparison of the results with experimental data is difficult at this stage of the calculations. Prevailing impurities in the material present are natural point defects Hg vacancies as acceptors and Hg interstitials as donors.[9] However, there is no reliable method to find the natural-defect concentration. In addition, the two scattering mechanisms used in the calculations are not sufficient to describe completely the transport in p-type $Hg_{1-x}Cd_xTe$. At least a disorder scattering should be included, too.

Taking that into account, we have only the indirect possibility to compare the KBE and BE results with experiment now. This is based on the estimate of the light-hole contribution to the Hall constant R_H. The effective light-hole part in R_H is given at low magnetic fields by a relative factor $\mathfrak{b}$ (Ref. 1)

$$\mathfrak{b}=\frac{r_H(2)p(2)[\mu(2)]^2}{r_H(1)p(1)[\mu(1)]^2}\ , \tag{42}$$

where $r_H(1), r_H(2)$ are heavy- and light-hole Hall scattering factors, respectively. This factor can be established experimentally from the magnetic-field dependence of R_H. Experimental data produce $\mathfrak{b}$ in an interval

TABLE III. Hole mobilities.

T (K)	KBE μ(1,I) (10^3 cm^2/V s)	KBE μ(2,I) (10^3 cm^2/V s)	KBE μ(1,II) (10^3 cm^2/V s)	KBE μ(2,II) (10^3 cm^2/V s)	BE μ(1,I) (10^3 cm^2/V s)	BE μ(2,I) (10^3 cm^2/V s)	BE μ(1,II) (10^3 cm^2/V s)	BE μ(2,II) (10^3 cm^2/V s)
10	7.4	43.3	2.42	20.9	2.12	141.0	0.68	33.8
15	8.8	45.4	2.45	16.6	2.98	179.0	0.77	39.7
20	10.4	51.0	2.55	14.9	3.86	207.0	0.88	48.9
30	10.9	60.0	2.66	13.3	4.88	220.0	1.07	59.0
40	7.4	47.1	2.40	11.7	4.18	180.0	1.12	56.0
60	2.65	19.7	1.54	8.0	2.00	85.0	0.86	37.0
80	1.29	9.9	1.00	5.5	1.04	42.5	0.60	22.9

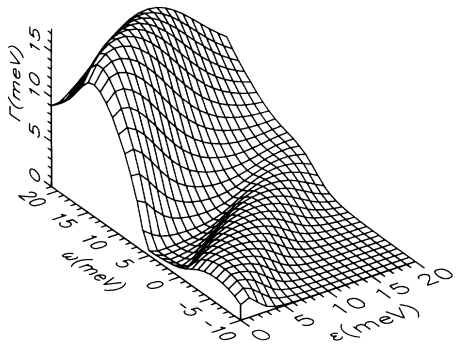

FIG. 6. Γ of the heavy-hole band in case I at temperature 40 K as a function of $\varepsilon[=k^2/(2m_1^*)]$ and ω.

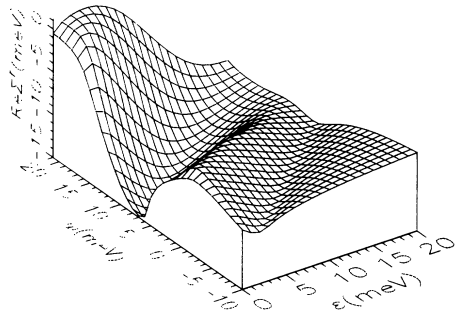

FIG. 7. $\mathrm{Re}\Sigma^r$ of the heavy-hole band in case I at temperature 40 K as a function of $\varepsilon[=k^2/(2m_1^*)]$ and ω.

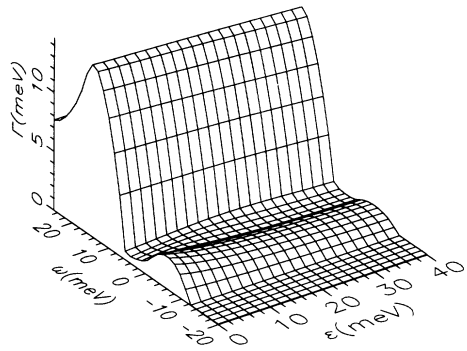

FIG. 8. Γ of the light-hole band in case I at temperature 40 K as a function of $\varepsilon[=k^2/(2m_2^*)]$ and ω.

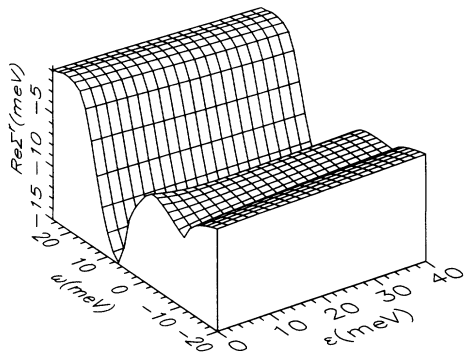

FIG. 9. $\mathrm{Re}\Sigma^r$ of the light-hole band in case I at temperature 40 K as a function of $\varepsilon[=k^2/(2m_2^*)]$ and ω.

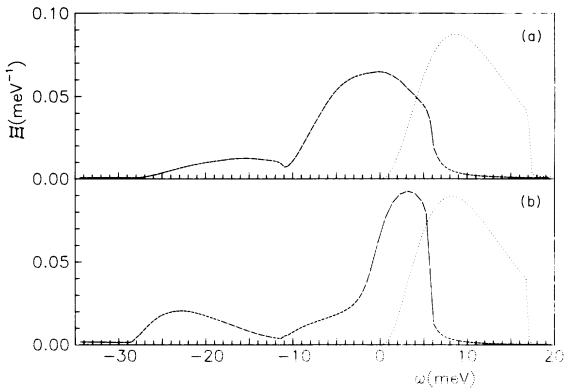

FIG. 10. Conduction rate in case I at temperature 40 K. Parts (a) and (b) depict the heavy- and light-hole rate, respectively. The dotted line shows the BE solution.

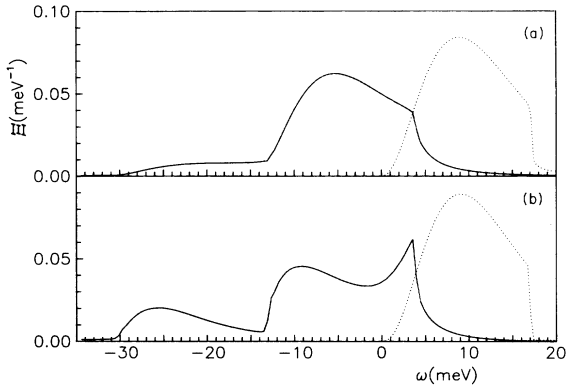

FIG. 11. Conduction rate at case II at temperature 40 K. Parts (a) and (b) depict the heavy- and light-hole rate, respectively. The dotted line shows the BE solution.

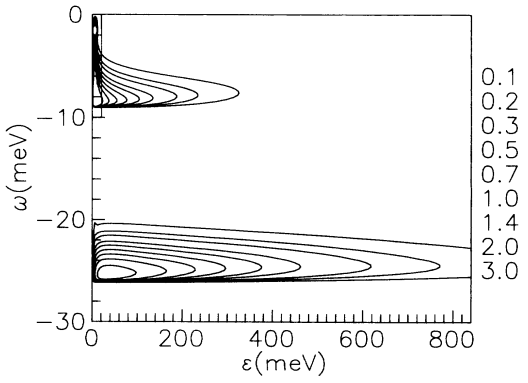

FIG. 12. The topographical projection of the light-hole conduction density in case I at temperature 10 K in units $[10^{-8}\ \Omega^{-1}\,\mathrm{cm}^{-1}\,\mathrm{meV}^{-2}]$. The numbers in the right column correspond to values of the individual constant value curves. The basis is at zero, the lower slings correspond gradually to the higher values.

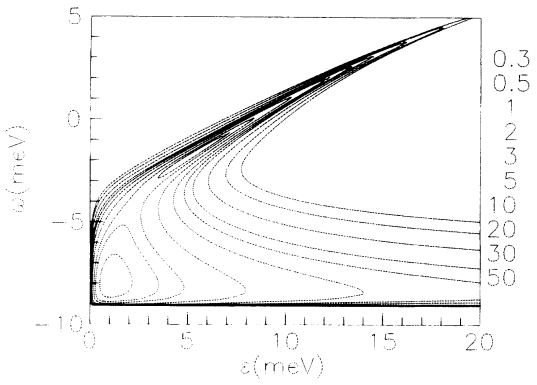

FIG. 13. The topographical projection of the light-hole conduction density. The detailed view of the outlined part of Fig. 12.

$\mathfrak{b}=0.3-0.7$.[1,15–17] Taking into account the simplification $r_H \approx 1$, we can easily compare experimental $\mathfrak{b}$ with the calculated results. Putting the data from Tables II and III into (42), we get theoretical $\mathfrak{b}$ in the interval 1.7–3 in the case of the BE and in the interval 0.07–0.3 in the case of the KBE. However, the comparison proposed here can be taken only as a preliminary result. Including the disorder scattering as well as other isotropic scattering mechanisms reduces $\mu(1)$ in (42) appreciably in comparison with $\mu(2)$. Also $r_H(1)$ results from the BE at low temperatures lower than $r_H(2)$ and one can expect the same relation also in the case of the KBE. Both these corrections should increase $\mathfrak{b}$ significantly. Consequently, the difference between the theory and experiment increases with including other (e.g., disorder) scatterings in the case of the BE and decreases in the case of the KBE. That is why we regard any such Kadanoff-Baym (-like) theory of the carrier mobility in narrow-gap materials indispensable.

TABLE IV. Relative echoes conductivity; the Boltzmann regime corresponds to $\hat{\gamma} \ll 1$.

T (K)	$\hat{\gamma}$ 1,I	$\hat{\gamma}$ 2,I	$\hat{\gamma}$ 1,II	$\hat{\gamma}$ 2,II
10	0.14	0.63	0.13	0.36
15	0.14	0.56	0.13	0.36
20	0.15	0.44	0.13	0.34
30	0.16	0.30	0.13	0.28
40	0.16	0.25	0.13	0.24
60	0.16	0.21	0.12	0.20
80	0.13	0.17	0.10	0.16

VIII. CONCLUSIONS

A more general formalism superseding the Boltzmann approach has been used to calculate the transport properties of p-type $Hg_{1-x}Cd_xTe$ semiconductors. Comparing with the Boltzmann theory, significant differences have been found in the density-of-states functions as in the mobilities calculated. A nonstandard effect of the transport in tails of the DOS owing to the renormalization effect of the scattering has been found which is especially strong in the light-hole band. Charged-impurity and optical-phonon scattering have been used. Inclusion of other scattering mechanisms is argued to amend (distort) agreement with experiment in the case of the KBE (BE) theory.

The results presented should be further extended to calculation of the transport properties at low magnetic fields in order to obtain the Hall constant and make a detailed comparison with experiment possible. Such calculations are in progress.

ACKNOWLEDGMENT

It is a pleasure to thank Dr. V. Čápek for many stimulating discussions and a critical reading of the manuscript.

[1]P. Höschl, P. Moravec, V. Prosser, R. Kužel, R. Grill, J. Franc, E. Belas, and Yu. M. Ivanov, J. Cryst. Growth. **101**, 822 (1990).
[2]L. P. Kadanoff and G. Baym, *Quantum Statistical Mechanics* (Benjamin, New York, 1962).
[3]E. O. Kane, in *Semiconductors and Semimetals*, edited by R. K. Willardson and A. C. Beer (Academic, New York, 1966), Vol. 1, p. 75.
[4]H. Ehrenreich, J. Phys. Chem. Solids **2**, 131 (1957); **9**, 129 (1959).
[5]J. D. Wiley, Phys. Rev. B **4**, 2485 (1971).
[6]G. D. Mahan, Phys. Rep. **145**, 251 (1987).
[7]R. Grill, Ph.D. thesis, Charles University, Prague, 1991.
[8]L. Y. Chen and Z. B. Su, Phys. Rev. B **40**, 9309 (1989).
[9]P. Höschl, P. Moravec, V. Prosser, V. Szöcs, and R. Grill, Phys. Status Solidi B **145**, 637 (1988).
[10]P. Höschl, P. Moravec, J. Franc, R. Grill, and E. Belas, J. Appl. Phys. **70**, 313 (1991).
[11]R. Grill, Phys. Status Solidi B **162**, 509 (1990).
[12]H. Sumi, J. Phys. Soc. Jpn. **36**, 770 (1974).
[13]V. Čápek and V. Špička, Czech. J. Phys. B **34**, 115 (1984).
[14]P. Höschl, P. Moravec, R. Grill, and V. Čápek, Phys. Status Solidi B **148**, 319 (1988).
[15]M. C. Gold and D. A. Nelson, J. Vac. Sci. Technol. A **4**, 2040 (1986).
[16]A. I. Elizarov, V. V. Kruzhaev, G. M. Minkov, M. S. Nikitin, and O. E. Rut, Phys. Tekh. Semiconduct. **21**, 472 (1987).
[17]P. S. Wijewarnasuriya, M. Boukerche, and J. P. Faurie, J. Appl. Phys. **67**, 859 (1990).